

Deuterium separation under ambient conditions by spatial confinement between Pd nanoparticles and benzene skeleton

Jingru Fu

Zhejiang Normal University

Saikat Das

Jilin University

Xiqi Zhang

Technical Institute of Physics and Chemistry, Chinese Academy of Sciences <https://orcid.org/0000-0001-5784-6734>

Ying Wang

Changchun Institute of Applied Chemistry, Chinese Academy of Sciences

Hongyan Xiao

Technical Institute of Physics and Chemistry, Chinese Academy of Sciences <https://orcid.org/0000-0003-1058-9149>

Teng Ben (✉ tengben@zjnu.edu.cn)

Zhejiang Normal University <https://orcid.org/0000-0002-0847-330X>

Lei Jiang

Technical Institute of Physics and Chemistry, Chinese Academy of Sciences <https://orcid.org/0000-0003-4579-728X>

Article

Keywords:

Posted Date: March 22nd, 2022

DOI: <https://doi.org/10.21203/rs.3.rs-1450218/v1>

License: © ⓘ This work is licensed under a Creative Commons Attribution 4.0 International License.

[Read Full License](#)

Deuterium separation under ambient conditions by spatial confinement between Pd nanoparticles and benzene skeleton

Jingru Fu^{1,2,3}, Saikat Das^{1,2,3}, Xiqi Zhang⁴, Ying Wang⁵, Hongyan Xiao⁴, Teng Ben^{1,2,3*},
Lei Jiang^{4,6*}

¹Zhejiang Engineering Laboratory for Green Syntheses and Applications of Fluorine-Containing Specialty Chemicals, Institute of Advanced Fluorine-Containing Materials, Zhejiang Normal University; Jinhua 321004, P. R. China. ²Department of Chemistry, Jilin University; Changchun 130012, P. R. China. ³Department of Chemistry, Jilin University, Changchun 130012, P. R. China. ⁴Key Laboratory of the Ministry of Education for Advanced Catalysis Materials, Institute of Physical Chemistry, Zhejiang Normal University, Jinhua 321004, P. R. China. ⁵CAS Key Laboratory of Bio-Inspired Materials and Interfacial Science, Technical Institute of Physics and Chemistry, Chinese Academy of Sciences; Beijing, 100190, P. R. China. ⁶State Key Laboratory of Rare Earth Resource Utilization, Changchun Institute of Applied Chemistry, Chinese Academy of Sciences; Changchun 130022, P. R. China. ^{*}School of Future Technology, University of Chinese Academy of Sciences; Beijing 100049, P. R. China. ^{*}Correspondence and requests for materials should be addressed to T.B. (email: tengben@zjnu.edu.cn) or to L.J. (jianglei@iccas.ac.cn).

Deuterium with high purity can be widely used in non-radioactive isotope tracking, neutron scattering and nuclear fusion. Current approaches for deuterium separation with Pd membrane and quantum sieving-based nanoporous materials are performed at high temperature (673 K) and ultralow temperature (30 K), respectively, both requiring high energy consumption but possessing low separation efficiency. However, efficient separation of deuterium under ambient conditions is still a remaining challenge. Here, we efficiently extract high-purity deuterium from an isotopic mixture under ambient conditions *via* spatial confinement between Pd nanoparticles and benzene skeleton, and reducing activation energy of the reaction. In-situ FT-IR results confirm that Pd nanoparticles (ca. 1.1 nm) in crystalline porous organic framework (CPOF-1) can chemically adsorb deuterium at room temperature. Density functional theory (DFT) calculations indicated that the spatial confinement effect reduces the reaction activation energy, and leads to Pd-deuterium reaction at room temperature. This study provides a new concept for deuterium separation with low energy consumption, low cost and high efficiency, and we envision that it could be of great significance in practical applications.

MAIN TEXT

Separation of hydrogen isotopes from their mixtures is substantially important in industrial and scientific research, with applications spanning nonradioactive isotopic tracer¹⁻³, neutron scattering⁴⁻⁶ and nuclear fusion⁷. The well-established approaches to hydrogen isotopes separation include kinetic quantum sieving (KQS)⁸⁻¹⁵ and chemical-affinity quantum sieving (CAQS)¹⁶⁻¹⁷ with microporous materials⁸⁻¹⁷; however, the separation requires ultra-low temperatures (e.g. 30 K for KQS, 77-100 K

41 for CAQS) which involves extensive energy consumption thus acting as a bottleneck to mass-
42 production of hydrogen isotopes. The industrial methods to prepare deuterium, namely, electrolysis of
43 deuterated water (D₂O) acquired through Girdler sulfide process¹⁸ and H₂ distillation¹⁹ are also highly
44 energy-intensive (**Table S4**), hence substantiating the importance of developing an energy-efficient
45 system that can directly extract high-purity deuterium (D₂) from isotope mixture under ambient
46 conditions.

47 From the standpoint of materials, porous materials on harnessing KQS effect have demonstrated
48 high-performance D₂/H₂ separation; nevertheless, preparing porous materials with appropriate pore
49 size and ultra-low temperature requirements costing huge energy consumption pose serious challenges.
50 On the contrary, Palladium (Pd) shows excellent hydrogen storage properties and Pd membranes can
51 purify hydrogen isotopes at high temperature (~673 K) by solution-diffusion mechanism²⁰; nonetheless,
52 this method is also greatly energy-consuming. In addition, although the two-dimensional crystal
53 membrane²¹ can separate high-purity hydrogen gas from the mixture of D₂/H₂, a product
54 predominantly containing high-purity deuterium is more favorable from an industrial viewpoint.
55 Therefore, efficient separation of deuterium at room temperature (298 K) and atmospheric pressure is
56 still a remaining challenge.

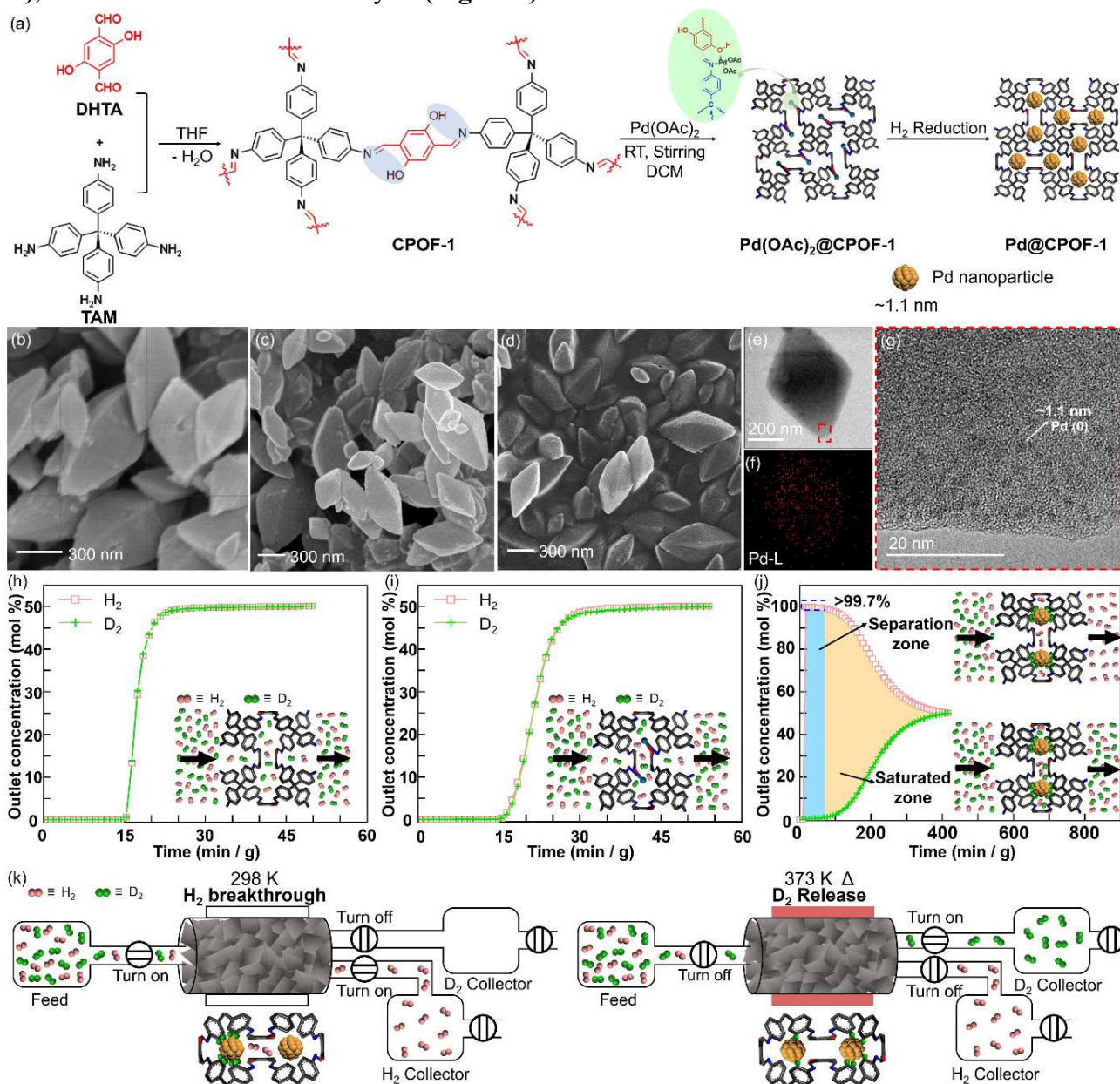
57 Here, a Pd and crystalline porous organic framework hybrid material (Pd@CPOF-1) is prepared,
58 which shows high-efficiency separation of hydrogen isotope mixtures under ambient conditions *via*
59 spatial confinement between Pd nanoparticle and benzene skeleton. Crystalline porous organic
60 framework (CPOF-1) is chosen considering its (i) abundant binding sites for Pd (II) and (ii) nanosize
61 pores, and Pd is chosen owing to the potential of Pd membranes to purify hydrogen isotopes. The
62 captive response of Pd nanoparticles in CPOF-1 pore channels reduce activation energy of the reaction,
63 which led to Pd reacting with D₂ at room temperature. This specially-designed nanoarchitecture
64 presents excellent D₂/H₂ breakthrough separation under ambient conditions. The synthesis scheme,
65 characterization and breakthrough performance are summarized in **Fig. 1**.

66

67 **Results and Discussion**

68 CPOF-1 was synthesized *via* Schiff base reaction between tetra-(4-anilyl)-methane and 2,5-
69 dihydroxyterephthalaldehyde in a mixture of tetrahydrofuran and 3 M aqueous acetic acid at 70 °C for
70 3 d. Considering the coordination between the active groups of -OH and imine bonds and metal ions
71 in the framework of CPOF-1, Pd(OAc)₂@CPOF-1 was synthesized by immersing Pd(OAc)₂ and
72 CPOF-1 in CH₂Cl₂ for 24 h and then the filter residue was treated by H₂ yielding Pd@CPOF-1 as a
73 reddish-brown powder (**Fig.1a**). In the 3d region of the X-ray photoelectron spectrum confirmed that
74 Pd²⁺ were successfully reduced to Pd⁰ by H₂, comparable to previous reports^{22,23} (**Fig. S11**). Based on
75 FT-IR and PXRD analyses, the chemical structure and crystalline of CPOF-1 was maintained without
76 collapse during introduction of Pd²⁺ into the CPOF pore channel and following reduction by hydrogen
77 (**Fig. S4, Fig. S7, Fig. S8**). Moreover, a new peak of Pd(0) could be found at 39.7° (2θ) in the PXRD
78 of Pd@CPOF-1, which is in accordance with XPS results. As per calculations based on the XRD
79 studies using the Scherrer equation, the size of these nanoparticles is ca. 1.3 nm. The microstructure
80 of CPOF-1 is characterized by SEM and TEM images, which showed octahedral crystal morphology
81 (**Fig.1b, Fig. S20**). After introduction of Pd(OAc)₂ and H₂ reduction, CPOF-1 retained its morphology
82 (**Fig. 1c-d, Fig. S20**). Energy dispersive X-ray spectroscopy (EDX) mapping analysis in TEM
83 exhibited uniform distribution of Pd in the crystals of Pd(OAc)₂@CPOF-1 and Pd@CPOF-1 (**Fig. 1e-**
84 **f, Fig. S21**). The well-dispersed palladium particles (black dots) could also be clearly observed in the

85 HR-TEM image and the average diameter of Pd(0) clusters inside the pores of CPOF-1 were about 1.1
 86 nm (**Fig. 1g, Fig. S23**), similar to XRD analysis. EDX analyses of Pd(OAc)₂@CPOF-1 and
 87 Pd@CPOF-1 revealed a loading of 2.2 wt% and 3.3 wt% for Pd (II) and Pd (0), respectively (**Fig. S24-**
 88 **25**), consistent with the TGA analysis (**Fig. S12**).



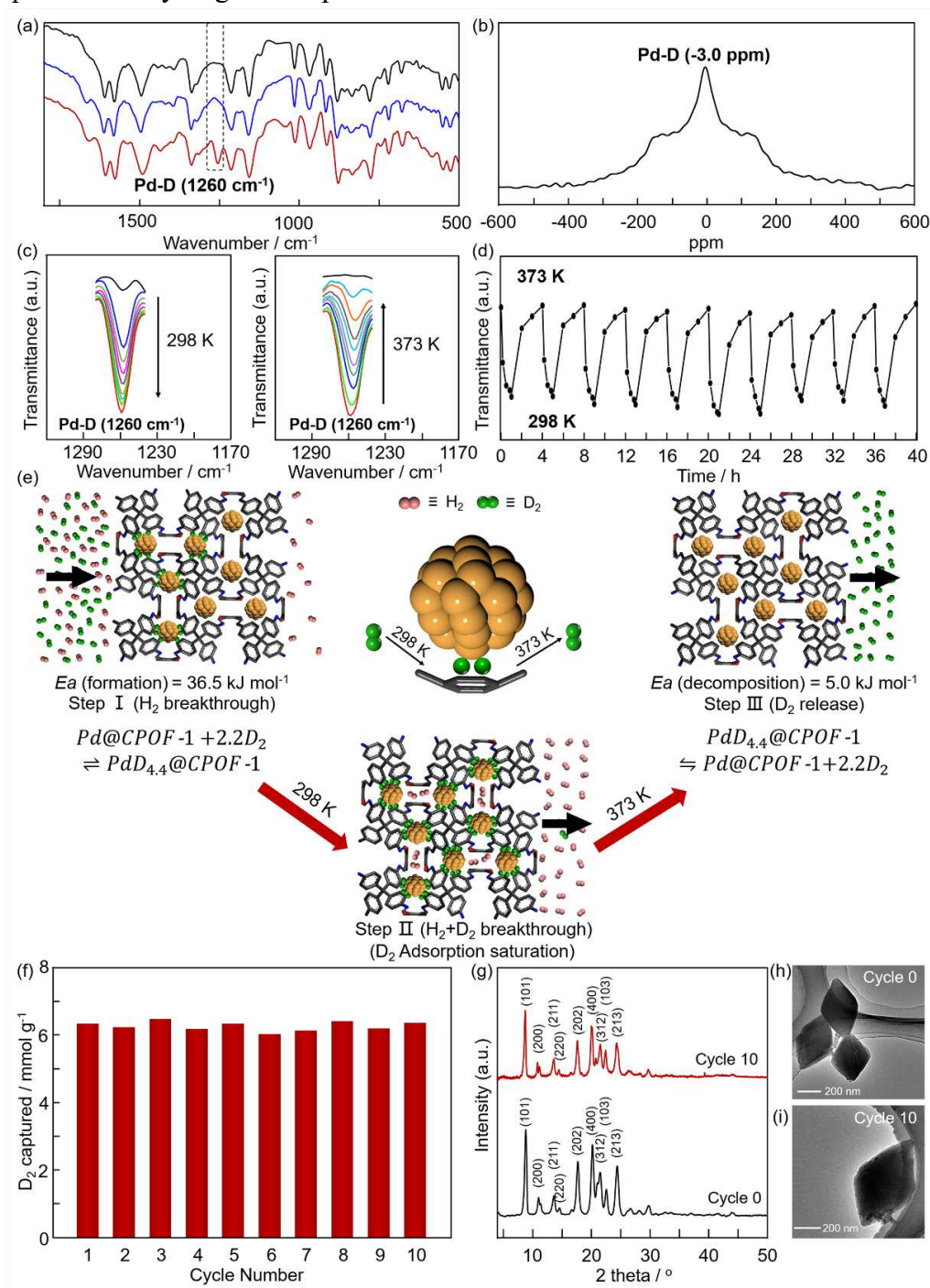
89
 90 **Figure 1 | Design, synthesis, and characteristics of the Pd@CPOF-1.** **a**, Schematic representation of the synthesis
 91 of CPOF-1, Pd(OAc)₂@CPOF-1 and Pd@CPOF-1 materials. SEM images of **b** CPOF-1, **c** Pd(OAc)₂@CPOF-1 and **d**
 92 Pd@CPOF-1. The morphology of CPOF-1 retained after introduction of Pd(OAc)₂ and H₂ reduction. **e**, **f**, EDX mapping
 93 image and **g** HR-TEM image of Pd@CPOF-1. Pd is highly dispersed in Pd@CPOF-1 and the size of Pd nanoparticles
 94 (dark dots) is about 1.1 nm, similar to XRD result (ca. 1.3 nm). Dynamic breakthrough curves for equimolar D₂/H₂
 95 mixture in a packed column with **h** CPOF-1, **i** Pd(OAc)₂@CPOF-1 and **j** Pd@CPOF-1 at 299 K, 1 bar (Breakthrough
 96 experiment schematic diagram respectively in insets). Due to the strong interaction between Pd@CPOF-1 and D₂,
 97 Pd@CPOF-1 showed excellent D₂/H₂ separation performance. By contrast, the CPOF-1 and Pd(OAc)₂@CPOF-1
 98 breakthrough experiments results indicated that no separation could be achieved. **K**, Schematic illustration of
 99 equimolar D₂/H₂ mixture separation in a packed column with Pd@CPOF-1. The samples (ca. 430 mg) were packed

100 into a stainless-steel column with a length of 10 cm and an inner diameter of 0.5 cm. Hydrogen with high-purity can
101 be obtained directly through single breakthrough cycle. The adsorbed D₂ in Pd@CPOF-1 can then be released by
102 heating, thus collecting high purity D₂. After one breakthrough cycle, the D₂ captured of Pd@CPOF-1 was 6.3 mmol
103 g⁻¹.

104
105 The breakthrough experiment is carried out in dynamic conditions, which is closer to the actual
106 industrial process. First, the breakthrough experiments of equimolar D₂/H₂ mixture for CPOF-1 and
107 Pd(OAc)₂@CPOF-1 were performed and results indicated that no separation could be achieved (**Fig.**
108 **1h, i**). To accurately assess the separation performance of Pd@CPOF-1 for equimolar D₂/H₂ mixture,
109 breakthrough experiments between 299 K and 353 K were performed (**Fig. 1j, Fig. S27**). As shown in
110 **Fig. 1j** and **Fig. 1k**, H₂ was first eluted through the fixed bed (Pd@CPOF-1, 430 mg) because of its
111 low adsorption capacity and weak affinity toward the adsorbent, and then high-purity H₂ product can
112 be directly collected. Besides, D₂ can be retained in the column for 97.8 min g⁻¹ with a highest capture
113 amount of 6.30 mmol g⁻¹ at 323 K (**Fig. S27, Table S2**). The D₂ uptake of Pd@CPOF-1 in our study
114 is especially higher than that of previously reported Py@COF-1 (0.50 mmol g⁻¹, 22 K)⁹, CC3 (3.67
115 mmol g⁻¹, 30 K)¹³, MOF-74-IM (2.80 mmol g⁻¹, 77 K)²⁴, MFU-4 (Zn, Cl) (0.02 mmol g⁻¹, 40 K)¹² and
116 FMOFCu (0.10 mmol g⁻¹, 25 K)¹¹ based on KQS or CAQS theory. As estimated from breakthrough
117 curves, 86.2 L of H₂ with over 99.7 % purity could be retrieved from an equimolar isotopic mixture
118 for 1 Kg of Pd@CPOF-1 within 30 mins at 323 K, which is higher than the productivity at other
119 temperatures (**Fig. S28**). Besides, hydrogen with a maximum purity of 99.98% can be obtained through
120 single breakthrough cycle at 323 K (**Table S3**). The sample was regenerated in-situ under high vacuum
121 for 3 h at 373 K before next measurements.

122 In order to further study the hydrogen isotope separation mechanism of Pd@CPOF-1, in-situ FT-IR
123 of Pd@CPOF-1 treated by Ar, H₂ and D₂ were explored (**Fig. 2a, Fig. S31-32**). Surprisingly, the FT-
124 IR spectrum of Pd@CPOF-1 under D₂ (**Fig. 2a**) showed a new and obvious characteristic absorption
125 peak at 1260 cm⁻¹ at 298 K, with other slight changes. But such phenomena could not be observed in
126 the Pd@CPOF-1 under H₂ atmosphere, so it was confirmed that D₂ is adsorbed chemically in
127 Pd@CPOF-1 while H₂ is adsorbed physically. Moreover, the above experimental results ruled out the
128 possibility of the $\sqrt{2}$ isotopic effect^{25,26}, indicating that the new characteristic absorption peak was Pd-
129 D bond and not caused by the redshifted D-D vibration of the adsorbed D₂. And the major peak (1260
130 cm⁻¹) was selected for further study. This Pd-D bond can be proved from ²H NMR spectra of
131 Pd@CPOF-1 after treated with deuterium at 298 K. A broad absorption line centered at -3.1 ppm was
132 observed (**Fig. 2b**), attributing to adsorbed deuterium atoms inside Pd lattice as hydride (Pd-D).
133 Notably, the chemical shift of Pd-D signal was little different from those reported in literature^{27,28},
134 which is due to different chemical environments caused by the confined effect of CPOF-1 channel.
135 Besides, the peak intensity gradually increased with increasing time (**Fig. 2c**), therefore suggesting a
136 new chemical bond was formed between D₂ guest molecules and Pd@CPOF-1. Furthermore, in-situ
137 FT-IR of Pd powder, Pd(OAc)₂@CPOF-1 and CPOF-1 under D₂ at 298 K revealed no new peak (**Fig.**
138 **S33-35**), suggesting that a new Pd-D bond was formed in the 1.8 nm pore channels of CPOF-1. Thus,
139 the predominant interaction between D₂ and Pd@CPOF-1 is not physisorption but Pd-D chemical
140 bonding. The Pd-D peak (1260 cm⁻¹) weakened and vanished at 373 K (**Fig. 2c**), showing its dynamic
141 bonding nature. Moreover, the Pd-D peak maintained strong intensity after ten cycles of formation and
142 decomposition, indicating high stability of Pd-D bond (**Fig. 2d**). Investigating temperature dependent
143 stop-flow experiment of in situ FTIR of Pd@CPOF-1 under D₂, the activation energy of Pd (clusters

144 inside the CPOF-1 channel) + 2.2 D₂ = PdD_{4.4} was determined to be 36.5 kJ mol⁻¹ at 295-333 K (**Fig.**
 145 **2e, Fig. S36, 37**) for D₂ coordinating, while the activation energy strikingly decreased to 5 kJ mol⁻¹ at
 146 343-373 K to allow D₂ recovering. Such phenomena cannot be observed in the Pd@CPOF-1 under H₂
 147 atmosphere (**Fig. S32**), indicating that H₂ was adsorbed into the pores of Pd@CPOF-1 via
 148 physisorption. Hence, chemically adsorbed D₂ and physically adsorbed H₂ show great adsorption-
 149 diffusion difference inside the channels of CPOF-1 at 298 K which resulted in marked D₂/H₂ selectivity
 150 under ambient conditions. We herein introduce the effect of spatial confinement that is promising for
 151 effective separation of hydrogen isotopes under ambient conditions.



152
 153 **Figure 2 | Deuterium separation mechanism of Pd@CPOF-1 and regenerability and stability of Pd@CPOF-1.**
 154 **a**, In-situ FT-IR spectra of activated Pd@CPOF-1 in Ar (black), H₂ (blue) and D₂ (red) atmosphere. Under 298 K and

155 D₂ atmosphere, a new infrared characteristic peak (Pd-D) appeared in Pd@CPOF-1, indicating that Pd nanoparticles
156 in the CPOF-1 nanochannel can react strongly with D₂ to form a stable Pd-d bond. **b**, Solid-state ²H NMR spectra for
157 Pd@CPOF-1 treated with deuterium gas. The Solid-state ²H NMR spectra confirmed the existence of Pd-D bond,
158 suggesting that Pd nanoparticles could react with D₂ at room temperature. **c**, The intensity of Pd-D bond as a
159 function of reaction time at 298 K and 373 K. Under 298 K and D₂ atmosphere, the strength of Pd-D bond gradually
160 increases with time, while the strength of Pd-D bond gradually weakened with time and can completely disappear
161 at 373 K, indicating that the formation of Pd-D bond is a reversible reaction. **d**, Cycling test of in-situ infrared for Pd-
162 D bond. Reaction at 298 K and D₂ atmosphere for one hour, followed by reaction at 373 K for three hours, namely
163 one cycle. After ten cycles, the strength of Pd-D bond almost the same, indicating a high stability. **e**, Hydrogen
164 isotope separation mechanism of Pd@CPOF-1. At 298 K, Pd nanoparticles selectively react with D₂ to form the Pd-
165 D bond in the confined space formed between Pd nanoparticles and benzene skeleton. At 373 K, the Pd-D bond
166 breaks and D₂ are released from Pd@CPOF-1. **f**, Recyclability of Pd@CPOF-1 in mixed gas column breakthrough
167 experiments for the equimolar D₂/H₂ mixture at 323 K and 1 bar. After ten breakthrough cycles, the D₂ captured
168 of Pd@CPOF-1 was almost the same. **g**, XRD patterns and **h**, **i** TEM images of Pd@CPOF-1 after breakthrough for
169 zero and tenth time. The crystal structure and morphology of Pd@CPOF-1 are maintained.

170

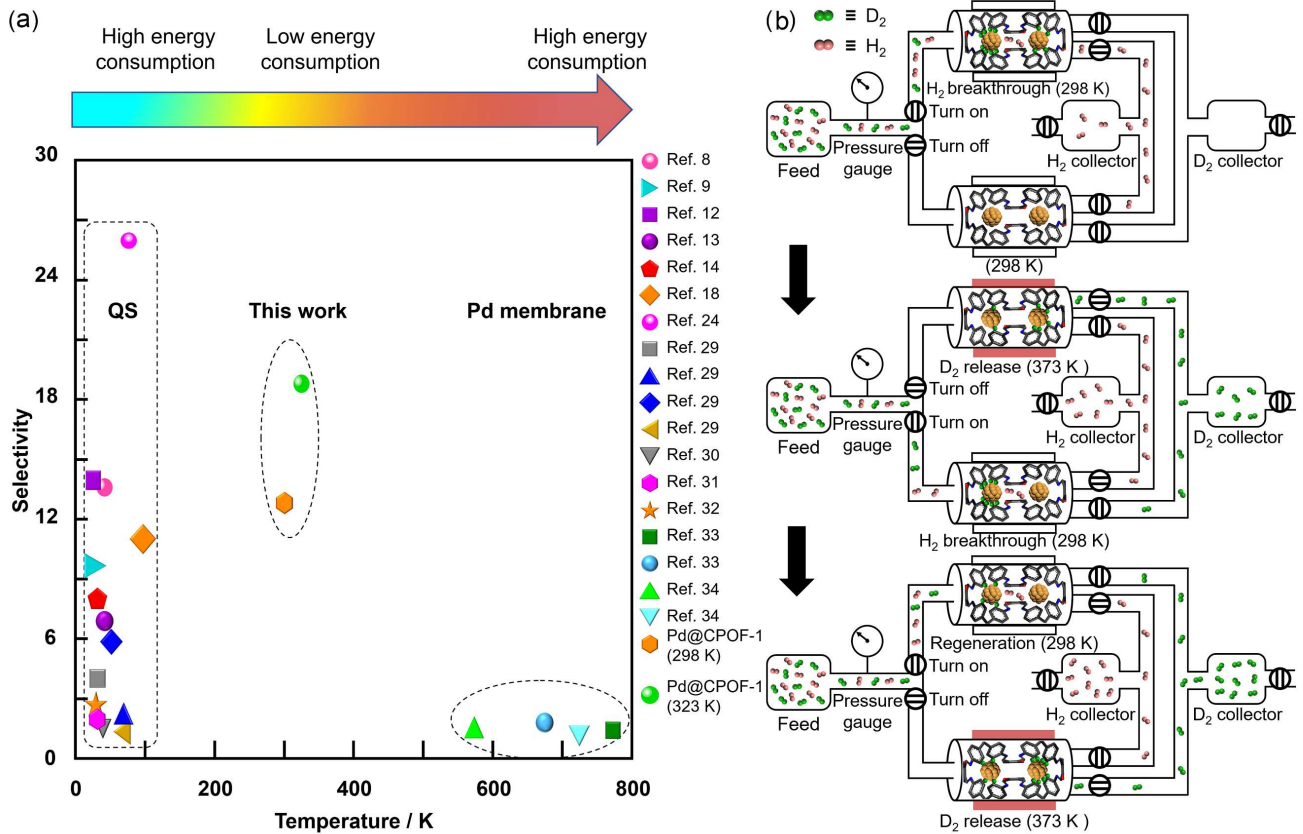
171 For practical industrial applications, the ideal adsorbent should have good recyclability and structural
172 stability. So, breakthrough experiments of H₂/D₂ mixture on Pd@CPOF-1 were tested ten times to
173 evaluate its cycle performance. As shown in **Fig. 2f** and **Fig. S29**, the breakthrough time and capture
174 capacity for D₂ were almost unchanged. Moreover, the crystallinity and morphology of Pd@CPOF-1
175 retained (**Fig. 2g-i**, **Fig. S9**, **Fig. S22**), indicative of the excellent regenerability and stability of
176 Pd@CPOF-1.

177 This is the first time the phenomenon of captivating Pd nanoparticles in the chemical space of CPOF-
178 1 leading to enhanced activity of the Pd nanoparticles lowering the activation energy was applied to
179 separate hydrogen isotopes at ambient conditions. Compared with other approaches, the spatial
180 confinement effect provides high selectivity, energy savings and efficiency (**Fig. 3a**). The efficiency
181 can be further improved by multi-stage separation, which makes this approach expected to be used in
182 practical applications (**Fig. 3b**).

183 Decrease of activation energy of Pd-D bond formation inside the organic frameworks due to the spatial
184 confinement effect can be explained by the density functional theory calculations and the frontier
185 molecular orbitals (FMO) theory³⁵. Compared D₂ with H₂, the energy barrier for generating 2D* on
186 Pd@ph-N (**Fig. 4a**) or Pd@ph-O (**Fig. S38**) is lowered by 0.10 eV, which might be an important reason
187 for improving the D₂ dissociation on Pd@CPOF-1 in kinetics. Furthermore, on the thermodynamics,
188 the reactions of D₂/H₂* → 2D/2H* on Pd@ph-N or Pd@ph-O are exothermic with 0.45-0.51 eV energy.
189 The reaction energy on Pd@ph-N or Pd@ph-O is ~0.4 eV lower than that on pristine Pd(111) (**Table**
190 **S6**). It indicates that the D₂/H₂* → 2D/2H* reaction is favorable to occur in the spatial confinement
191 system.

192 Further, the HOMO of the benzene skeleton and the *d_{xz}* of palladium symmetrically matched LUMO
193 of D₂/H₂ in the narrow gap (~3.5 Å), which decrease the vibration and rotation of the confined D₂/H₂
194 molecule hence leading to decrease activation energy of Pd-D formation at room temperature (**Fig. 4b-**
195 **c**). The activation energy of forming Pd-H should decrease as the case of Pd-D but still required higher
196 temperature to trigger the reaction, which allow D₂/H₂ separation at ambient temperature.

197



198

199

200

201

202

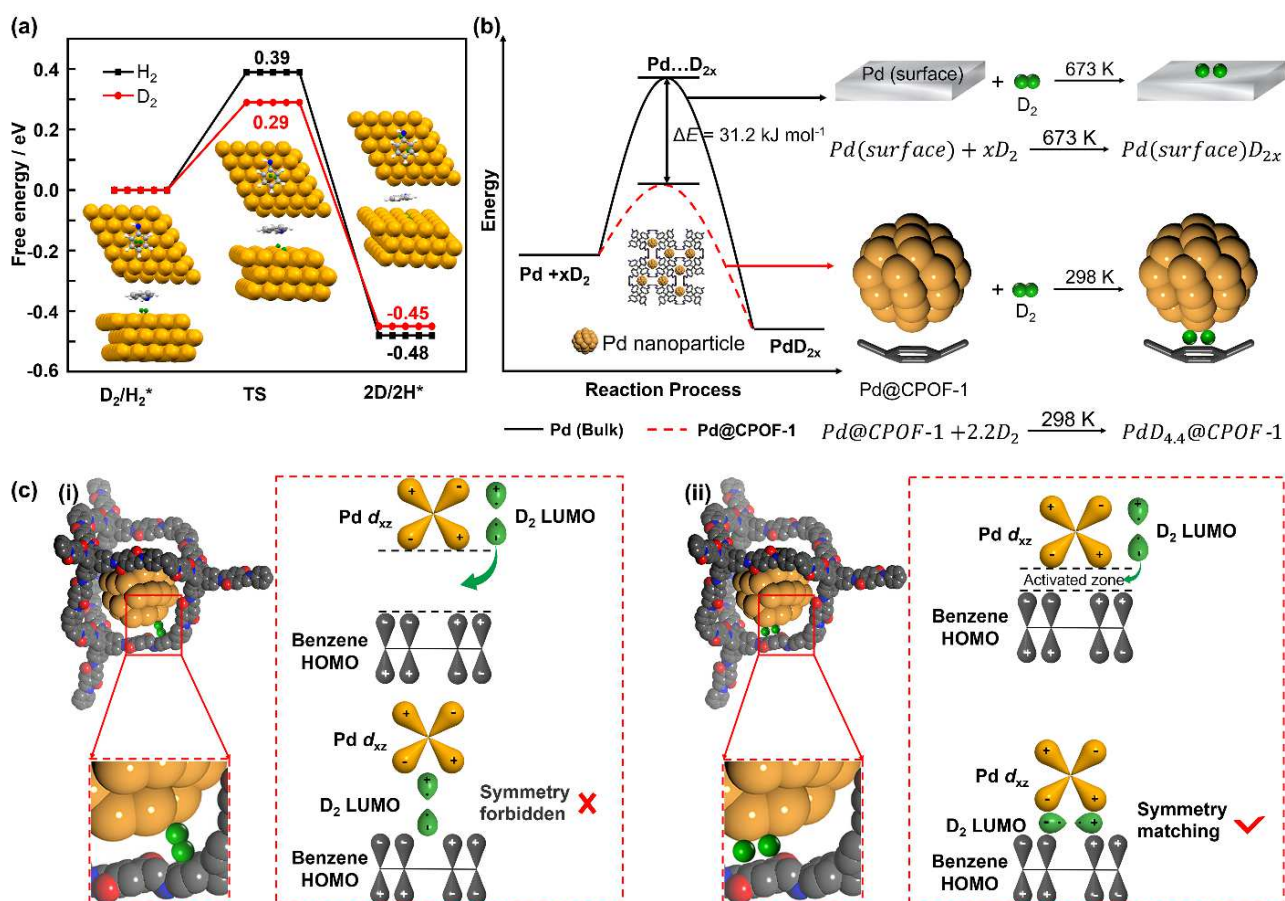
203

204

205

206

Figure 3 | Pd@CPOF-1 exhibits excellent hydrogen isotope separation performance. **a**, Hydrogen isotope separation factors as a function of working temperature. The hydrogen isotope separation methods use Pd membrane or QS based nanoporous materials realize only at high temperature or ultralow temperature, respectively, both of which are high energy consumption. In contrast, Pd@CPOF-1 can achieve efficient hydrogen isotope separation with low energy consumption under mild conditions. (QS stands for quantum sieving, including KQS and CAQS). **b**, Schematic diagram of multistage hydrogen isotope separation device. We envision a multistage separation device with potential industrial applications. Through multi-level parallel connection, the separation time can be saved, and continuous separation can be realized, thus improving the separation efficiency.



207

208

209

210

211

212

213

214

215

216

217

218

219

220

221

222

223

224

225

226

227

228

229

Figure 4 | Reaction mechanism of Pd@CPOF-1 with deuterium. **a**, Free energy diagrams of $D_2/H_2^* \rightarrow 2D/2H^*$ on Pd@ph-N. The yellow brown, green, white, blue, and grey balls are Pd, D, H, N, and C atoms, respectively. **b**, Spatial confinement effect plays a decisive role in the reaction between Pd@CPOF-1 and D_2 . The confined effect of CPOF-1 nanochannels enhanced the reaction activity of Pd nanoparticles by lowering the reaction activation energy. Based on the spatial confinement effect formed between Pd nanoparticles and benzene skeleton, Pd nanoparticles reacted with D_2 at 298 K to form the Pd-D bond. In comparison, the reaction of D_2 at Pd surface take place at a much higher temperature of 673 K. **c**, Frontier molecular orbitals theory provides insights into the mechanism for the reaction of Pd@CPOF-1 and D_2 . (i) D_2 enters the confined space formed between Pd nanoparticle and benzene skeleton, and when the d_{xz} of palladium and the LUMO of D_2 is symmetry forbidden, the reaction between Pd nanoparticle and D_2 cannot occur without additional energy. (ii) In the confined space formed between Pd nanoparticle and benzene skeleton, when the HOMO of the benzene skeleton and the d_{xz} of palladium symmetrically matched LUMO of D_2 in the narrow gap, Pd nanoparticles will directly react with D_2 to form the Pd-d bond.

Conclusions

In summary, we present a specially-designed Pd@CPOF-based construct that can effectively separate high-purity deuterium from isotopic mixture under ambient conditions *via* the spatial confinement between Pd nanoparticle and benzene skeleton, and reducing activation energy of the reaction. Unlike KQS and CAQS, this approach is about captivating Pd nanoparticles in the framework of the CPOF that contributes to increased activity of the Pd nanoparticles lowering the activation energy thereby allowing chemisorption of D_2 at room temperature. Chemically adsorbed D_2 and physically adsorbed H_2 showed pronounced adsorption-diffusion difference inside the pore channels of Pd@CPOF-1 facilitating outstanding D_2/H_2 selectivity at room temperature. This study presents a

230 sustainable approach of implementing custom-made porous materials to pioneer state-of-the-art
231 isotope separation systems.

232

233 **Methods**

234 **Characterizations.** The FTIR spectroscopy was performed with a SHIMADZU IRAffinity-1 Fourier transform
235 infrared spectrophotometer. The solid-state ^{13}C cross-polarization magic-angle-spinning (CP/MAS) NMR spectra
236 was recorded on a BRUKER AVANCEIII 400 WB solid-state spectrometer. The XRD measurements were done using
237 SHIMADZU XRD-6000 X-ray diffractometer with Cu-K α radiation and scanning rate of $0.6^\circ \text{ min}^{-1}$ (2θ). The
238 thermogravimetric analysis (TGA) was done using a SHIMADZU DTG-60 thermal analyzer at a heating rate of 10
239 $^\circ\text{C min}^{-1}$ to 800°C in a dried air atmosphere with air flow rate of 30 mL min^{-1} . Scanning electron microscopy (SEM)
240 was performed with JEOS JSM-6700 scanning electron microscope. The transmission electron microscopy (TEM)
241 images were obtained on JEM-2100 transmission electron microscopy. The low-pressure gas adsorption
242 measurements were done with Micro Meritics TristarII 3020 surface area and pore size analyzer. The contents of Pd
243 element in CPOF-1 were analyzed by SPECTRO BLUE SOP Inductively coupled plasma emission spectrometer
244 (ICP-OES). XPS spectra were obtained using the ESCALAB250Xi X-ray Photoelectron Spectrometer (XPS). Solid-
245 state ^2H NMR spectra was collected using a BRUKER AVANCEIII HD-400 NMR spectrometer. Regarding cycling
246 test of in-situ infrared for Pd-D bond, each cycle takes four hours, with the first hour of testing at 298 K and three
247 hours at 373 K .

248

249 **Synthesis of Pd@CPOF-1.** The activated $\text{Pd}(\text{OAc})_2$ @CPOF-1 were treated with pure hydrogen (99.999%) at 1 bar
250 and 80°C . After 4 h of treatment, the samples were washed with H_2O and acetone to remove the liberated
251 acetylacetonate ligands and then were thoroughly dried at 80°C under vacuum for 12 hours to obtain Pd@CPOF-1.
252 The Pd content in Pd@CPOF-1 were $0.9 \text{ wt}\%$, $1.7 \text{ wt}\%$, $2.9 \text{ wt}\%$ as determined by ICP. A series of Pd@CPOF-1 with
253 different Pd content ($0.9\text{-}2.9 \text{ wt}\%$) was prepared with the highest palladium doping amount determined as high as 2.9
254 $\text{wt}\%$ that showed best D_2/H_2 separation performance (**Fig. S26**). So, the optimized Pd@CPOF-1 ($2.9 \text{ wt}\%$) will be
255 selected for further study.

256 **Fourier Transform Infrared (FT-IR) spectra.** The infrared test of Pd@CPOF-1 in D_2 atmosphere was taken as an
257 example. Prior to infrared test, KBr and Pd@CPOF-1 were taken in a $50:1$ ratio, mixed thoroughly and then ground
258 using a mortar and pestle in the glove box. Then a certain amount of the mixture was taken onto one Al_2O_3 pan and
259 pressed using the iron bar to form pellet. Under the argon atmosphere, the Al_2O_3 pan was quickly loaded into the
260 infrared test chamber filled with argon. Prior to the measurement of the time dependence of Pd-D bond infrared
261 spectra, D_2 with a flow rate of 8 mL min^{-1} was injected into the sample chamber for 5 s , and the sample was exposed
262 to D_2 atmosphere with a pressure of 1.0 bar for at least 25 s . Finally, the data were collected at different time intervals.
263 The preparation process of KBr sample for FT-IR test was similar to that of Pd@CPOF-1. Background data was
264 collected in the D_2 atmosphere. The temperature was controlled in situ by the heating device.

265 Fourier Transform Infrared (FT-IR) spectrum of CPOF-1 showed a characteristic peak at 1620 cm^{-1} which was
266 assigned to $\text{C}=\text{N}$ stretching, indicating successful reaction between aldehyde and amine groups (**Fig. S3** in
267 Supplementary Information). Based on FT-IR analyses (**Fig. S4**), the chemical structure of CPOF-1 was maintained
268 without collapse during introduction of Pd^{2+} into the CPOF pore channel and following reduction by hydrogen.

269 As shown in **Fig. S31a**, the FT-IR spectrum of Pd@CPOF-1 under D_2 showed a new characteristic absorption peak
270 at 1260 cm^{-1} at 298 K , but such phenomena cannot be observed in the Pd@CPOF-1 under H_2 atmosphere when H_2
271 was selected the reference for D_2 spectra, indicating that Pd@CPOF-1 had different adsorption behaviors with H_2
272 and D_2 . In addition, when we used D_2 as the reference for the H_2 spectra (**Fig. S30b**), this is, exposing Pd@CPOF-1
273 to D_2 atmosphere first and H_2 atmosphere later, the infrared spectra spectrum hardly changed and the characteristic

274 absorption peak at 1260 cm⁻¹ maintained.

275

276 **Solid-state ¹³C NMR spectra.** The solid-state ¹³C cross-polarization magic-angle-spinning (CP/MAS) NMR
277 spectrum showed a characteristic peak at 159 ppm, confirming the formation of C=N (**Fig. S5**).

278

279 **Powder X-ray diffraction (PXRD) pattern.** To characterize the crystallinity and crystalline structure of the novel
280 CPOF-1, PXRD was measured. As shown in **Fig. S6**, powder X-ray diffraction (PXRD) pattern of CPOF-1 exhibited
281 sharp and intense diffraction peaks at 8.78°, 10.03°, 13.46°, 14.32°, 17.81°, 20.33°, 21.79°, 22.63° and 24.85° which
282 can be assigned to (101), (200), (211), (220), (202), (400), (312), (103), and (213) Bragg peaks, indicating high
283 crystallinity. The crystalline structure and unit cell parameters of CPOF-1 were analyzed from the PXRD patterns
284 combined with structural simulations. After a geometrical energy minimization using Materials Studio software
285 package³⁶ based on different degrees of interpenetrated *dia* net respectively, the simulation clearly suggested that the
286 CPOF-1 is proposed to adopt a 5-fold interpenetrated *dia* topology with *I-42d* space group (**Fig. S10, Table S5**).
287 Pawley refinement yielded a PXRD that is in good agreement with experimentally observed pattern ($a = b = 20.25$
288 Å, $c = 14.03$ Å, $\alpha = \beta = \gamma = 90.0^\circ$, $R_{wp} = 9.60$ %, and $R_p = 6.21$ %).

289

290 **X-ray photoelectron spectroscopy (XPS).** In the 3d region of the X-ray photoelectron spectrum (XPS, **Fig. S11**) of
291 Pd(OAc)₂@CPOF-1, two characteristic peaks at 337.6 eV and 343.0 eV could be observed, which can be assigned
292 to 3d_{5/2} and 3d_{3/2} states of Pd²⁺. After reduced by hydrogen, Pd@CPOF-1 showed characteristic peaks at 336.5 eV
293 (3d_{5/2}) and 342.0 eV (3d_{3/2}) of Pd⁰, comparable to previous reports^{22,23}.

294

295 **Thermogravimetric analysis (TGA) curves.** The TGA plots of the samples (activated CPOF-1, Pd(OAc)₂@CPOF-
296 1 and Pd@CPOF-1) was achieved from a SHIMADZU DTG-60 thermal analyzer at a heating rate of 10 °C min⁻¹ to
297 800 °C in a dried air atmosphere with air flow rate of 30 mL min⁻¹. The Al₂O₃ pan was selected and used to load the
298 samples.

299 The TGA (**Fig. S12**) suggested that CPOF-1, Pd(OAc)₂@CPOF-1 and Pd@CPOF-1 possess good thermal stability
300 up to 423, 300 and 286 °C, respectively.

301

302 **Low-pressure gas sorption measurements.** The N₂, H₂ and D₂ adsorption-desorption isotherms were obtained from
303 Micro Meritics TristarII 3020 surface area and pore size analyzer. N₂ adsorption test was carried out at 77 K (liquid
304 nitrogen). The adsorption-desorption isotherms of H₂ and D₂ were measured at 77 K (liquid nitrogen), 87 K (liquid
305 helium), 298 K (water bath), 303 K, 308 K, 313 K, 318 K, and 323 K. H₂ and D₂ isotherms at 303 K, 308 K, 313 K
306 and 323 K using the heating jacket program to keep the temperature stable. The sample (80 mg) was vacuumed and
307 dried at 100 °C for 12 hours before the test. The used gases had the following purities: H₂ (99.999%), D₂ (99.99%),
308 N₂ (99.999%).

309 The surface areas and pore size distributions of CPOF-1, Pd(OAc)₂@CPOF-1 and Pd@CPOF-1 were determined
310 from N₂ adsorption analysis (**Fig. S13**). Type I pattern sorption isotherms were observed and the Brunauer-Emmett-
311 Teller (BET) surface areas were calculated as 1066, 113 and 109 m² g⁻¹ for CPOF-1, Pd(OAc)₂@CPOF-1 and
312 Pd@CPOF-1, respectively. Analyzed by nonlocal density functional theory (NLDFE), the pore size distributions of
313 CPOF-1, Pd(OAc)₂@CPOF-1 and Pd@CPOF-1 were 1.8, 1.3 and 1.5 nm, respectively. H₂ and D₂ adsorption
314 isotherms obtained from Pd@CPOF-1 exhibited hysteresis between 273 K and 323 K (**Fig. S14-15**), indicating high
315 interaction between guest gas molecules and Pd@CPOF-1³⁷. The amount of gas absorbed at 1 bar showed a
316 maximum at 303 K for both gases (**Table S1**). At 298 K and 1 bar, the H₂ and D₂ adsorption capacities were 0.84
317 mmol g⁻¹ and 0.72 mmol g⁻¹, which were 17 and 14 times greater than that of CPOF-1 (H₂: 0.05 mmol g⁻¹; D₂: 0.05

318 mmol g⁻¹) (Fig.S14). However, the H₂ and D₂ uptake on Pd@CPOF-1 at 77 K and 87 K was lower than that of CPOF-
 319 1 (Fig. S16, 17), due to the decrease of specific surface area and pore volume after Pd loading. Hence, the contribution
 320 of Pd nano-particles to the H₂ and D₂ storage capacity is negligible at low temperature.
 321 Alongside, Pd sponge exhibited reversible isotherms (Fig. S18), suggesting weak interaction of hydrogen with Pd
 322 sponge compared to that with Pd nano-particles captivated in the pores of CPOF-1. Contrasting from the case of Pd
 323 sponge, D₂ was chemisorbed by Pd@CPOF-1 and the coordination number of Pd/D was determined as 4.4 based on
 324 D₂ uptake at 298 K, indicating the formation of PdD_{4.4} inside the confined channels of CPOF-1 (Fig. S2).

325
 326 **Ideal adsorbed solution theory (IAST).** The selectivity of D₂/H₂ mixture from pure H₂ and D₂ isotherm was
 327 predicted through using ideal adsorbed solution theory (IAST) of Myers and Prausnitz³⁸. Single H₂ and D₂ isotherms
 328 were fitted with a Dual-Site Langmuir (DSL) model, given by the following equation:

$$329 \quad N = A_1 \frac{b_1 P}{1+b_1 P} + A_2 \frac{b_2 P}{1+b_2 P} \quad (1)$$

330 Where N stands for the adsorbed amount (mmol g⁻¹); A_1 and A_2 represent the adsorption saturation capacity for
 331 site 1 and site 2 respectively (mmol g⁻¹); b_1 and b_2 are dimensionless Langmuir parameters for site 1 and site 2; P
 332 stands for the pressure of the bulk at equilibrium with the adsorbent phase (kPa).

333 Then the binary adsorption selectivity of D₂/H₂ (1:1) in a mixture of H₂ and D₂ can be defined by Eq. (2):

$$334 \quad S = \frac{q_1/q_2}{P_1/P_2} \quad (2)$$

335 Where S stands for the ideal selectivity of D₂ over H₂, q_1 and q_2 are the molar loadings in the adsorbent in
 336 equilibrium (mmol g⁻¹); P_1 and P_2 are the pressure (kPa).

337 Based on the single-component isotherms of H₂ and D₂ of Pd@CPOF-1 (Fig. S14-15), the selectivity of D₂/H₂ (1/1)
 338 mixture were estimated to be 12.8 and 18.8 under almost zero coverage at 298 K and 323 K by applying ideal
 339 adsorbed solution theory (IAST) (Fig. S19).

340
 341 **Dynamic column breakthrough experiment.** Column breakthrough experiments were conducted in an in-house
 342 lab-scale fixed-bed system. The breakthrough separation apparatus is shown in Fig. S1. The samples (ca. 430 mg)
 343 were packed into a stainless-steel column with a length of 10 cm and an inner diameter of 0.5 cm. A carrier gas (N₂)
 344 was used to purge the adsorbent for 12 h at room temperature. Then a gas mixture of H₂/D₂/N₂ (1/1/2, vol%) at a total
 345 flow rate of 2.4 mL min⁻¹ was allowed to flow into the column at 299 K and 1 bar. The test temperature can be
 346 controlled by the heating system. The component concentrations of the outlet gas were monitored continuously by a
 347 mass spectrometer (Pfeiffer Vacuum Omnistar GSD 320). After each breakthrough experiment, the sample was
 348 regenerated in situ under high vacuum for 3 h at 373 K before the next measurement. The used gases had the following
 349 purities: H₂ (99.999%), D₂ (99.99%), N₂ (99.999%).

350
 351 **Adsorption capacity calculation based on breakthrough data.** For D₂/H₂ mixture component breakthrough the D₂
 352 uptake in the adsorbent can be obtained as follows^{39,40}:

$$353 \quad Q = M_{max} - M_c \quad (3)$$

$$354 \quad M_{max} = a_{D_2} \times \left(\tau - \int_0^\infty f(\tau) d\tau \right) \quad (4)$$

$$355 \quad \tau = \frac{t \times q}{v_m \times m} \quad (5)$$

356 Where Q stands for the D₂ uptake in the adsorbent (mmol g⁻¹); M_{max} represents the amount of D₂ retained on
 357 the column at a particular specific injection amount τ (mmol g⁻¹) at equilibrium, M_c is the amount of D₂ residing

358 in the free space of the pipeline and the column (mmol g^{-1}); t is the time that the $\text{H}_2/\text{D}_2/\text{N}_2$ mixture passes through
359 the packed column (min); q is the flow of inlet D_2 (mL min^{-1}); m stands for the quality of activated sample filled
360 in the sample column (g), a_{D_2} is the percent of D_2 in the mixture; $V_m=22.4 \text{ L mol}^{-1}$.

361

362 **The working process of a multistage hydrogen isotope separation device.** In this work, a simple two-stage parallel
363 device was taken. First, when the equimolar D_2/H_2 mixture enters the device, the inlet switch of the first fixed-bed
364 was turned on and the switch connecting the H_2 collector was turned on. At this time, D_2 is adsorbed in the
365 Pd@CPOF-1 filled in the fixed-bed and the high purity H_2 penetrates out and is collected. After the H_2 collection
366 was finished, the inlet switch of the first fixed-bed and the H_2 collector was turned off, the switch of D_2 collector was
367 turned on, and the fixed-bed at 373 K was heated so that D_2 was released from it and high purity D_2 was collected. At
368 the same time, the inlet switch of the second fixed-bed and the H_2 collector switch was turned on to collect H_2 . In
369 this way, H_2 and D_2 can be collected at the same time without time limitation, leading to achieve continuous separation
370 and improve the separation efficiency (**Fig. 3b**). If the device can be equipped with more steps, the separation
371 efficiency will be higher.

372

373 **Density functional theory calculations.** The geometric and energetic calculations were performed by density
374 functional theory (DFT) with Vienna ab-initio simulation package (VASP)⁴¹⁻⁴⁴. The interactions between ion cores
375 and valence electrons were described by projector augmented wave (PAW) method^{45,46}. The generalized gradient
376 approximation with the Perdew-Burke-Ernzerhof was adopted as the exchange-correlation functional⁴⁷. The wave
377 functions at each k-point were expanded with a plane wave basis set. The kinetic cutoff energy was set to 400 eV.
378 The integration of the Brillouin zone was conducted using a $1 \times 1 \times 1$ Monkhorst-Pack grid⁴⁸. The geometry structures
379 were optimized using a force-based conjugate-gradient method⁴⁴ until the energy was converged to 1.0×10^{-4}
380 eV/atom and the force to 0.05 eV/\AA . Spin polarization and vdW (Van der Waals) with vdW-DF approximation⁴⁹ were
381 considered in the current study. The transition states (TS) were obtained by the climbing image nudged elastic band
382 method⁵⁰.

383 The Pd@CPOF-1 was constructed by cutting the bulk Pd along (111) direction and 5×5 supercell with three layers
384 was selected as the computational model. Since CPOF-1 is too large, to balance the computational time and accuracy,
385 ph-N and ph-O radicals or molecules were put on the Pd(111) surface to simulate the interaction between Pd and
386 CPOF-1, as shown in **Fig. S39**. During the optimization the atoms in the last layer were fixed to maintain the bulk
387 structure and the other atoms were allowed to fully relax. A vacuum layer of 15 \AA was used along the c direction
388 normal to the surface to avoid periodic interactions.

389 The free energy diagrams of D_2/H_2 dissociation were estimated by the following equation:

$$390 \quad \Delta G = \Delta E + \Delta ZPE - T\Delta S \quad (6)$$

391 Where ΔE is the energy difference of reactants and products or transition states; ΔZPE and ΔS are the energy
392 difference of zero-point energy and entropy; T is the temperature, here 298.15 K is considered. Zero-point energies
393 and entropies are obtained from the vibrational frequencies.

394

395 **Acknowledgements**

396 This study was supported by the National Key R&D program of China (No. 2021YFA1200400), the National Natural
397 Science Foundation of China (No. 91956108, 21871103 and 51973227), the Natural Science Foundation of Zhejiang
398 Province (No. LZ22B010001), and the Youth Innovation Promotion Association CAS (No. 2020028). Part of the
399 computational time is supported by the High Performance Computing Center of Jilin University and Jilin Province,
400 as well as Network and Computing Center of Changchun Institute of Applied Chemistry, Chinese Academy of
401 Sciences.

402

403 **Author contributions**

404 T.B. was responsible for the design, direction and supervision of the project. J.F. performed the experimental work.
405 T.B., L.J., J.F. and S.D. analyzed and discussed the experimental results and drafted the manuscript. X.Z. participated
406 in data analysis and discussion and offered useful suggestions. Y.W and H.X performed the density functional theory
407 calculations.

408

409 **Additional information**

410 Supplementary information is available in the online version of the paper. Reprints and permissions information is
411 available online at xxx. Correspondence and requests for materials should be addressed to T.B. or to L.J.

412

413 **Competing financial interests**

414 The authors declare no competing financial interests.

415

416 **Data availability**

417 The authors declare that the data supporting the findings of this study are available within the Article and its
418 Supplementary Information or from the corresponding author upon reasonable request.

419

420 **References**

- 421 1 Stiopkin, I. V. *et al.* Hydrogen bonding at the water revealed by isotopic dilution spectroscopy. *Nature* **474**, 192-
422 195 (2011).
- 423 2 Povinec, P. P. *et al.* Isotope tracing of submarine groundwater discharge offshore Ubatuba, Brazil: results of the
424 IAEA–UNESCO SGD project. *J. Environ. Radioact.* **99**, 1596-1610 (2008).
- 425 3 Kerr, W. J. *et al.* Iridium-catalysed *ortho*-H/D and -H/T exchange under basic conditions: C–H activation of
426 unprotected tetrazoles. *Chem. Commun.* **52**, 6669-6672 (2016).
- 427 4 Zaccai, G. How soft is a protein? A protein dynamics force constant measured by neutron scattering. *Science* **288**,
428 1604-1607 (2000).
- 429 5 Büldt, G., Gally, H. U., Seelig, A., Seelig, J. & Zaccal, G. Neutron diffraction studies on selectively deuterated
430 phospholipid bilayers. *Nature* **271**, 182-184 (1978).
- 431 6 Machida, A. *et al.* Site occupancy of interstitial deuterium atoms in face-centred cubic iron. *Nat. Commun.* **5**, 5063
432 (2014).
- 433 7 Sanderson, K. Big interest in heavy drugs. *Nature* **458**, 269-269 (2009).
- 434 8 Kim, J. Y. *et al.* Selective hydrogen isotope separation via breathing transition in MIL-53 (Al). *J. Am. Chem. Soc.*
435 **139**, 17743-17746 (2017).
- 436 9 Oh, H. *et al.* A cryogenically flexible covalent organic framework for efficient hydrogen isotope separation by
437 quantum sieving. *Angew. Chem. Int. Ed.* **52**, 13219-13222 (2013).
- 438 10 Niimura, S. *et al.* Dynamic quantum molecular sieving separation of D₂ from H₂-D₂ mixture with nanoporous
439 materials. *J. Am. Chem. Soc.* **134**, 18483-18486 (2012).
- 440 11 Zhang, L. D. *et al.* Exploiting dynamic opening of apertures in a partially fluorinated MOF for enhance H₂
441 desorption temperature and isotope separation. *J. Am. Chem. Soc.* **141**, 19850-19858 (2019).
- 442 12 Teufel, J. *et al.* MFU-4 –A metal-organic framework for highly effective H₂/D₂ separation. *Adv. Mater.* **25**, 635-
443 639 (2013).
- 444 13 Liu, M. *et al.* Barely porous organic cages for hydrogen isotope separation. *Science* **366**, 613-620 (2019).
- 445 14 Chen B. L. *et al.* Surface interactions and quantum kinetic molecular sieving for H₂ and D₂ adsorption on a mixed

446 metal-organic framework material. *J. Am. Chem. Soc.* **130**, 6411-6423 (2008).

447 15 Si, Y. N., Wang, W. j., EI-Sayed, EI-Sayed. M. & Yuan, D. Q. Use of breakthrough experiment to evaluate the
448 performance of hydrogen isotope separation for metal-organic frameworks M-MOF-74 (M=Co, Ni, Mg, Zn). *Sci*
449 *China Chem* **63**, 881-889 (2020).

450 16 FitzGerald, S. A., Pierce, C. j., Rowsell, J. L. C., Bloch, E. D. & Mason, J. A. Highly selective quantum sieving
451 of D₂ from H₂ by a metal-organic framework as determined by gas manometry and infrared spectroscopy. *J. Am.*
452 *Chem. Soc.* **135**, 9458-9464 (2013).

453 17 Weinrauch, I. *et al.* Capture of heavy hydrogen isotopes in a metal-organic framework with active Cu (I) sites.
454 *Nat. Commun.* **8**, 14496 (2017).

455 18 Rae, H. K. in *Separation of Hydrogen Isotopes* (Symposium Series, ACS, 1987), vol. 68, chap. 1, pp. 1-26.

456 19 Keyser, G. M., McConnell, D. B., Anyas-Weiss, N. & Kirkby, P. in *Separation of Hydrogen Isotopes* (ACS, 1987),
457 vol. 68, pp. 126-133.

458 20 Glugla, M., Cristescu, I. R., Cristescu, I. & Demange, D. Hydrogen isotope separation by permeation through
459 palladium membranes. *J. Nucl. Mater.* **355**, 47-53 (2006).

460 21 Lozada-Hidalgo, M. *et al.* Sieving hydrogen isotopes through two-dimensional crystals. *Science* **351**, 68-70 (2016).

461 22 Tong, X., Zhao, Y. X., Huang, T., Liu, H. F. & Liew, K. Y. Controlled synthesis of pompon-like self-assemblies of
462 Pd nanoparticles under microwave irradiation. *Appl. Surf. Sci.* **255**, 9463-9468 (2009).

463 23 Pachfule, P. *et al.* Multifunctional and robust covalent organic framework-nanoparticle hybrids. *J. Mater. Chem.*
464 *A.* **2**, 7944-7952 (2014).

465 24 Kim, J. Y. *et al.* Exploiting diffusion barrier and chemical affinity of metal-organic framework for efficient
466 hydrogen isotope separation. *J. Am. Chem. Soc.* **139**, 15135-15141 (2017).

467 25 FitzGerald, S. A., Mukasa, D., Rigdon, K. H., Zhang, N. Y. & Barnett, B. R. Hydrogen isotope separation within
468 the metal-organic framework Cu(I)-MFU-4l. *J. Phys. Chem. C* **123**, 30427-30433 (2019).

469 26 FitzGerald, S. A., Forth, S. & Rinkoski, M. Induced infrared absorption of molecular hydrogen in solid C60. *Phys.*
470 *Rev. B* **65**, 140302(R) (2002).

471 27 Dekura, S. *et al.* The electronic state of hydrogen in the α phase of the hydrogen storage material PdH(D)_x: Does
472 a chemical bond between palladium and hydrogen exist? *Angew. Chem. Int. Ed.* **57**, 9823-9827 (2018).

473 28 Kobayashi, H. *et al.* On the nature of strong hydrogen atom trapping inside Pd nanoparticles. *J. Am. Chem. Soc.*
474 **130**, 1828-1829 (2008).

475 29 Teufel, J. Experimental investigation of H₂/D₂ isotope separation by cryoadsorption in metal-organic frameworks.
476 thesis, Universität Stuttgart (2013).

477 30 Savchenko, I. *et al.* Hydrogen isotope separation in metal-organic frameworks: kinetic or chemical affinity
478 quantum-sieving? *Microporous Mesoporous Mater.* **216**, 133-137 (2015).

479 31 Mondal, S. S. *et al.* Systematic experimental study on quantum sieving of hydrogen isotopes in metal-amide-
480 imidazolate frameworks with narrow 1-D channels. *ChemPhysChem* **20**, 1311-1315 (2019).

481 32 Xiong, R. J. *et al.* Thermodynamics, kinetics and selectivity of H₂ and D₂ on zeolite 5A below 77K. *Microporous*
482 *Mesoporous Mater.* **264**, 22-27 (2018).

483 33 Luo, D. L., Xiong, Y. F., Song, J. F. & Huang, G. Q. Hydrogen isotope separation factor measurement for single
484 stage hydrogen separators and parameters for a large-scale separation system. *Fusion Sci Technol.* **48**, 156-158
485 (2005).

486 34 Luo, D. L., Shen, C. S. & Meng, D. Q. Hydrogen isotope separation factors on palladium alloy membranes. *Fusion*
487 *Sci Technol.* **41**, 1142-1145 (2002).

488 35 Fukui, K., Yonezawa, T. & Shingu, H. A Molecular orbital theory of reactivity in aromatic hydrocarbons. *J. Chem.*
489 *Phys.* **20**, 722-725 (1952).

490 36 Materials Studio ver. 7.0; Accelrys Inc.; San Diego, CA.
491 37 Malouche, A., Zlotea, C. & Szilágyi, P. Á. Interactions of hydrogen with Pd@MOF composites. *ChemPhysChem*
492 **20**, 1282-1295 (2019).
493 38 Myers, A. L. & Prausnitz, J. M. Thermodynamics of mixed-gas adsorption. *AIChE J.* **11**, 121-127 (1965).
494 39 Lin, R. B. *et al.* Molecular sieving of ethylene from ethane using a rigid metal-organic framework. *Nat. Mater.* **17**,
495 1128-1133 (2018).
496 40 Liao, P. Q. *et al.* Putting an ultrahigh concentration of amine groups into a metal-organic framework for CO₂
497 capture at low pressure. *Chem Sci.* **7**, 6528-6533 (2016).
498 41 Liao, P. Q. *et al.* Putting an ultrahigh concentration of amine groups into a metal-organic framework for CO₂
499 capture at low pressure. *Chem Sci.* **7**, 6528-6533 (2016).
500 42 Kresse, G. & Hafner, J. *Ab initio* molecular dynamics for liquid metals. *Phy. Rev. B.* **47**, 558-561 (1993).
501 43 Kresse, G. & Hafner, J. *Ab initio* molecular-dynamics simulation of the liquid-metal–amorphous-semiconductor
502 transition in germanium. *Phys. Rev. B* **49**, 14251-14269 (1994).
503 44 Kresse, G. & Furthmuller, J. Efficient iterative schemes for ab initio total-energy calculations using a plane-wave
504 basis set. *Phys. Rev. B* **54**, 11169-11186 (1996).
505 45 Blochi, P. E. Projector augmented-wave method. *Phy. Rev. B* **50**, 17953-17979 (1994).
506 46 Kresse, G. & Joubert, D. From ultrasoft pseudopotentials to the projector augmented-wave method. *Phys. Rev. B*
507 **59**, 1758-1775 (1999).
508 47 Perdew, J. P., Burke, K. & Ernzerhof, M. Generalized Gradient Approximation Made Simple. *Phys. Rev. Lett.* **77**,
509 3865-3868 (1996).
510 48 Monkhorst, H. J. & Pack, J. D. Special Points for Brillouin-Zone Integrations. *Phys. Rev. B* **13**, 5188-5192 (1976).
511 49 Dion, M., Rydberg, H., Schröder, E., Langreth, D. C. & Lundqvist, B. I. Van der Waals Density Functional for
512 General Geometries. *Phys. Rev. Lett.* **92**, 246401 (2004).
513 50 Henkelman, G., Uberuaga, B. P. & Jonsson, H. A climbing image nudged elastic band method for finding saddle
514 points and minimum energy paths. **113**, 9901-9904 (2000).

515
516
517
518
519
520
521
522

Supplementary Files

This is a list of supplementary files associated with this preprint. Click to download.

- [supplementarymaterials.docx](#)